Solar Energy 225 (2021) 494–500

Contents lists available at ScienceDirect

Solar Energy

journal homepage: www.elsevier.com/locate/solener

Analysis of grain orientation and defects in Sb_2Se_3 solar cells fabricated by close-spaced sublimation

R. Krautmann [a,*], N. Spalatu [a,*], R. Gunder [b], D. Abou-Ras [b], T. Unold [b], S. Schorr [b,c], M. Krunks [a], I. Oja Acik [a]

[a] Tallinn University of Technology, Department of Materials and Environmental Technology, Laboratory of Thin Film Chemical Technologies, Ehitajate tee 5, 19086 Tallinn, Estonia
[b] Helmholtz-Zentrum Berlin für Materialien und Energie GmbH, Department Structure and Dynamics of Energy Materials, Hahn-Meitner Platz 1, 14109 Berlin, Germany
[c] Freie University Berlin, Institute of Geological Sciences, Malteserstr. 74-100, 12249 Berlin, Germany

ARTICLE INFO

Keywords:
Antimony selenide
Close-spaced sublimation
Grain orientation
Pole figures
Deep defects
Admittance spectroscopy

ABSTRACT

The performance of a superstrate TiO_2/Sb_2Se_3 solar cell, fabricated by close-spaced sublimation technique (CSS), was improved after the deployment of a seed layer. The seed layer caused columnar Sb_2Se_3 film growth with texture coefficient analysis (TC) showing increased presence of crystal planes, which are inclined towards the [001] crystal direction. Given the highly anisotropic properties of Sb_2Se_3, preferential growth of $(Sb_4Se_6)_n$ ribbons along the [001] direction is best suited for effective charge collection. Hence, grain orientation of Sb_2Se_3 films was studied more closely via measurement of pole figures by XRD and orientation distribution maps by electron backscatter diffraction (EBSD). Although the measurements did not reveal strong preferred orientation, it was observed that the columnar Sb_2Se_3 growth enhanced texture along the [001] direction. Temperature-dependent admittance spectroscopy (TAS) and capacitance–voltage (CV) profiling were performed on the seed-assisted TiO_2/Sb_2Se_3 solar cell to evaluate carrier density and deep defects in the Sb_2Se_3 absorber. TAS study revealed a deep defect with activation energy of 0.39 eV. CV profiles indicated that the density of defects could be as high as 10^{17} cm^{-3}, which needs to be addressed by post-deposition treatments.

1. Introduction

Antimony selenide (Sb_2Se_3) has emerged as a potential photovoltaic absorber. Sb_2Se_3 has excellent optoelectronic properties: a high absorption coefficient (>10^5 cm^{-1} at shorter wavelengths) (Zhou et al., 2014) and suitable band-gap of 1.1–1.3 eV (Li et al., 2019c; Wen et al., 2018). Single phase binary structure and low evaporation point have made Sb_2Se_3 compatible with CdTe solar cell fabrication processes (Spalatu et al., 2017), also partly explaining the rapid growth in Sb_2Se_3 solar cell efficiency. While deposition techniques, such as magnetron sputtering (Liang et al., 2020) and rapid thermal evaporation (RTE) (Chen et al., 2017b) have allowed fabrication of Sb_2Se_3 devices with >6% efficiency, close-spaced sublimation (CSS) and vapor transport deposition (VTD) techniques have enabled to produce champion Sb_2Se_3 solar cells with efficiencies 9.2% (Li et al., 2019c) and 7.6% (Wen et al., 2018), respectively. Recently, Spalatu et al., reported on the optimization of growth conditions for depositing Sb_2Se_3 absorber layers by CSS, in which the Sb_2Se_3 layers deposited at 450 °C onto the TiO_2 buffer layer saw optimal performance (Spalatu et al., 2021). This involved use of a seed layer, which significantly improved the microstructure of the Sb_2Se_3 absorber. In order to better understand the current limitations of CSS-deposited Sb_2Se_3 devices, the microstructure and defect properties are investigated in more detail in this work. This paper aims to give a significantly more accurate account on the orientations of polycrystalline Sb_2Se_3 films and shed light on the physical origin and role of one of the deep defects prevalent in the Sb_2Se_3 absorber.

Lately, a lot of attention has turned to the crystal anisotropy. Sb_2Se_3 possesses orthorhombic crystal structure, where crystals form one-dimensional (1D) $(Sb_4Se_6)_n$ ribbons, in which atoms are covalently bonded (Ghosh, 1993; Liu et al., 2014). At the same time, ribbons adjacent to each other only bond via weak van der Waals' forces. After proving that the carrier transport is more efficient along the covalently bonded $(Sb_4Se_6)_n$ ribbons than between them (Chen et al., 2017a), it became clear that carrier collection could be significantly improved provided that Sb_2Se_3 grains are preferentially grown along the *c*-axis, [001] crystal direction. To illustrate this, record Sb_2Se_3 solar cell

* Corresponding authors.
E-mail addresses: robert.krautmann@taltech.ee (R. Krautmann), nicolae.spalatu@taltech.ee (N. Spalatu).

https://doi.org/10.1016/j.solener.2021.07.022
Received 28 April 2021; Received in revised form 28 June 2021; Accepted 12 July 2021
Available online 29 July 2021

performance (η = 9.2%) was largely attributed to the nanoribbons exhibiting preferred orientation in the *c*-axis direction (Li et al., 2019c). Today, links between preferred orientation and device performance have been demonstrated in many studies, and are mainly proven through texture coefficient (TC) analysis derived from the XRD patterns (Li et al., 2019a, 2017; Liang et al., 2020; Wang et al., 2017; Zhang et al., 2020; Zhou et al., 2020). By definition, TC value that is larger than 1 indicates a preferred orientation of a *hkl* reflection compared with the random distribution of grains in a powder (Bérubé and L'Espérance, 1989). Previously, it has been argued that the TC analysis might not be best suited for measuring texture in polycrystalline films with highly anisotropic crystallites, because the grain morphology could contribute to the overestimation of the actual texture (Ariosa et al., 2011). More recently, however, TC analysis was argued to be a trustable tool for evaluating preferred orientation in Sb_2Se_3 films, because the outcome was consistent with what was observed from pole figures measured by XRD (Pattini et al., 2020). Considering the above, pole figure measurements by XRD and orientation distribution maps by electron-backscatter diffraction (EBSD) were performed in addition to the TC analysis with the aim to provide more clarity regarding the grain orientation of the Sb_2Se_3 films.

While favorable Sb_2Se_3 grain orientations enhance charge transport, numerous deep defects in Sb_2Se_3 trap and prevent carriers from being collected. A large $V_{OC} > 0.7$ V deficit poses one of the many bottlenecks, explaining why Sb_2Se_3 devices are still far from the theoretical efficiency limit (Savory and Scanlon, 2019). For bandgaps of 1.1–1.3 eV, studies have reported V_{OC} values between 0.36 and 0.43 V (Hobson et al., 2020; Li et al., 2019b, 2019c; Wang et al., 2017; Wen et al., 2018). Significant levels of recombination via deep traps can in large part explain the low V_{OC} (Savory and Scanlon, 2019). Wen et al., were first to demonstrate multiple trap states deep in the band gap using deep-level transient spectroscopy (DLTS) (Wen et al., 2018). First-principles calculations by Huang et al., and Liu et al., also suggested that Sb_2Se_3 has large concentrations of multiple defects, especially antisite defects, e.g. Sb_{Se}, Se_{Sb} and $2Se_{Sb}$, that are located deep in the band gap (Huang et al., 2019; Liu et al., 2017). So far, there are only few admittance studies in the literature exploring deep defects in Sb_2Se_3 devices. Chen et al., used temperature-dependent admittance spectroscopy (TAS) together with temperature-dependent conductivity measurements and found activation energies of 96 meV and 111 meV, respectively (Chen et al., 2017a). These defect energy levels were ascribed to a Se_{Sb} antisite defect. Hu et al., has reported activation energies at 352 meV, 495 meV and 526 meV, only ascribing the highest obtained energy to an interface defect (Hu et al., 2019, 2018b). Wang et al., demonstrated two defects with activation energies of 356 meV and 423 meV (Wang et al., 2020). Tang et al., reported two activation energies of 456 meV and 495 meV assigning these to V_{Se} and Sb_{Se}, respectively (Tang et al., 2019). Comparison of these studies shows significant discrepancies between the reported activation energies and the assignments to certain types of defects. Thus, further work is needed to elucidate the defect structure of Sb_2Se_3.

This study presents a close analysis of grain orientation and defects in Sb_2Se_3 solar cells fabricated by close-spaced sublimation. XRD measurements were combined with advanced pole figure and electron backscatter diffraction measurements to study the grain growth and orientation in the absorber. The role of seed layer on the Sb_2Se_3 film structure and orientation is also discussed. Furthermore, TAS and CV profiling are performed to estimate the carrier density and potential deep defects. Better understanding of the Sb_2Se_3 film growth and defects helps to refine processing steps for tackling the dominant recombination processes, which are vital for improving Sb_2Se_3 device performance.

2. Experimental

2.1. Fabrication of Sb_2Se_3 thin film and solar cell

Soda-lime glass substrates with a 200 nm thick 20 Ω sq^{-1} fluorine-doped tin oxide (FTO) were used. TiO_2 films with a thickness of 100 nm were deposited onto FTO by ultrasonic spray pyrolysis at 340 °C (Eensalu et al., 2019). A precursor solution was used, where 0.1 M titanium isopropoxide (TTIP) and acetylacetone (1:4 M ratio) were dissolved in ethanol. Next, substrates were vacuum annealed at 120 °C and air-annealed at 450 °C for 30 min. Sb_2Se_3 absorber films were deposited from a Sb_2Se_3 powder (5 N, Sigma-Aldrich) using close-spaced sublimation (CSS) setup under vacuum level of 10^{-4} Pa. A 60 nm thick Sb_2Se_3 seed layer was first deposited at 300 °C. Next, Sb_2Se_3 film with ~1.8 μm thickness was deposited at 450 °C. Au back contacts with square area of 25 mm^2 were vacuum evaporated through a Mica mask onto Sb_2Se_3 absorber films.

2.2. Sb_2Se_3 thin film characterization

Sb_2Se_3 absorber films were imaged by Zeiss EVO-MA15 scanning electron microscope (SEM) equipped with a Zeiss HR FESEM Ultra 55 system. X-ray diffraction (XRD) patterns were measured using a Rigaku Ultima IV diffractometer with Cu Kα radiation (λ = 1. 54 Å, 40 kV, 40 mA). Texture analysis was performed by PANalytical MRD X-ray diffractometer equipped with Eulerian cradle employing two-axis scans along φ and χ in increments of 5° each. The intensity distribution was recorded along full circles (φ = 0° to 360°) and at sample tilts χ ranging between 0° and 85°. Electron backscatter diffraction (EBSD) orientation maps were acquired using a Zeiss UltraPlus scanning electron microscope equipped with an Oxford Instruments Symmetry EBSD detector. The measurements were conducted at a beam energy of 20 keV and a beam current of about 6nA, by use of the acquisition and evaluation software AZtec.

2.3. Device characterization

J-V curves were measured using an AUTOLAB PGSTAT 30 and an Oriel class A solar simulator 91159A (100 mW cm^{-2}, AM1.5) in ambient air at room temperature. The external quantum efficiency (EQE) spectra were measured using a monochromatized light source (Newport 300 W Xenon lamp, 69911 with a monochromator Newport Cornerstone 260), a Merlin digital lock-in detector and a factory-calibrated Si reference detector. Capacitance-voltage (CV) profiling was performed at room temperature with a HP 4284 LCR meter at frequencies ranging from 0.5 kHz to 20 kHz and 30 mV ac voltage. DC bias was scanned from –0.3 V to 0 V. Temperature dependent admittance measurements were made with a HP 4284 LCR meter in R–X (resistance–reactance) mode at 0 V bias and 30 mV ac voltage. Frequency was varied from 0.1 kHz to 1 MHz. Temperature was varied from 80 K to 320 K.

3. Results and discussion

3.1. Analysis of Sb_2Se_3 grain orientation

The film structure of Sb_2Se_3 films was characterized by scanning electron microscopy (SEM). Under investigation were two structures: (1) Sb_2Se_3 with a seed layer (labelled as 'Sb_2Se_3 + SL'; see Experimental section) between TiO_2 buffer and Sb_2Se_3 absorber and (2) Sb_2Se_3 without seed layer. Cross-sectional SEM images of these two structures are shown in Fig. 1. Sb_2Se_3 + SL film, as shown in Fig. 1b, possesses a more compact structure as compared to the Sb_2Se_3 without seed layer in Fig. 1a. When comparing the two absorber films, it is likely the seed layer laid the groundwork for producing columnar grains and increased compactness.

Improved growth of Sb_2Se_3 has been explained by seed layer creating

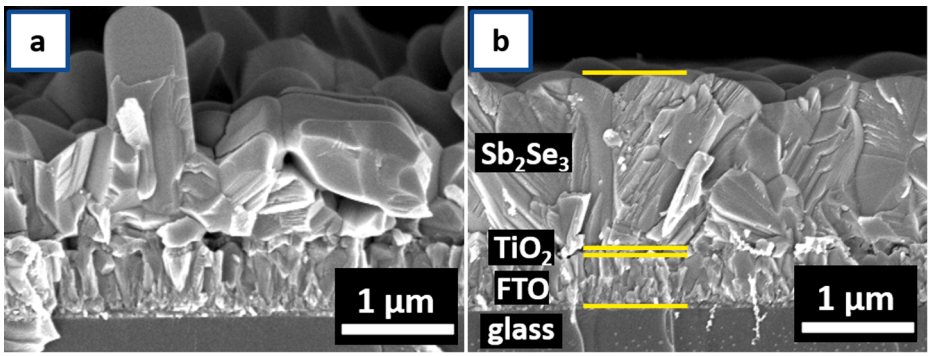

Fig. 1. Cross-sectional SEM image of Sb_2Se_3/TiO_2/FTO/glass structures where in (a) Sb_2Se_3 absorber was grown without seed layer and in (b) Sb_2Se_3 absorber was grown onto seed layer.

ribbon-like seeds that start coalescing into columnar grains during the subsequent deposition process (Spalatu et al., 2021). Due to strong re-sublimation at 450 °C CSS processing, only a small number of seeds, from which grains evolve, remain active on the surface. This explains why the seed layer cannot be distinguished from Fig. 1b.

The two structures were then characterized by XRD to determine the crystal structure of Sb_2Se_3 films. As seen from Fig. 2a, Sb_2Se_3 films exhibit crystal structure with orthorhombic *Pbnm* space group symmetry (JCPDS 15–0861); no secondary crystal phases were detected. To examine variation in crystal orientation, texture coefficient (TC) was calculated from Eq. (1):

$$TC(hkl) = \frac{I(hkl)}{I_0(hkl)} \times \left[\frac{1}{N}\sum_{i=0}^{N}\frac{I(h_ik_il_i)}{I_0(h_ik_il_i)}\right]^{-1} \quad (1)$$

where *I(hkl)* is the intensity obtained experimentally for a given reflection with *hkl* indices, $I_0(hkl)$ is the reference intensity for the corresponding reflection acquired from the JCPDS Card No. 15–0861, and *N* is the number of reflections considered in the calculations (Bérubé and L'Espérance, 1989).

Calculated TC values are presented in Fig. 2b, revealing that both Sb_2Se_3 films with and without seed layer have lower TC values for (hk0) planes than for (hk1) planes. When comparing the two films, it can be noted that the TC values for (hk0) planes are always lower in Sb_2Se_3 + SL. Given that the 221 and 231 planes show higher TC values, this could imply more Sb_2Se_3 crystals are orienting along the *c*-axis direction, which is reportedly beneficial for charge transport (Li et al., 2019c). Noteworthy is also the difference between TC values found for the 002 peak. While Sb_2Se_3 + SL reaches TC of 1.2 for the (002) plane, the corresponding value for Sb_2Se_3 without seed layer stands low at 0.2. Knowing that the 002 peak refers to vertical Sb_2Se_3 crystals, high TC values shared between the 221, 231, and 002 planes could indicate that the Sb_2Se_3 + SL might grow preferentially along the [001] direction. To further study the grain orientation, advanced texture measurements were subsequently conducted.

Fig. 3 displays pole figures of the Sb_2Se_3 absorbers in 020 and 002 projections measured by XRD. Each pole figure is provided with an intensity scale, where the intensity correlates directly to the multiple of random distribution (MORD). Larger is the multiple of random distribution, stronger is the texture (strong texture translates into preferred orientation) (Abou-Ras et al., 2018). It was noted that Sb_2Se_3 without seed layer showed stronger intensity for the 020 peak, while Sb_2Se_3 + SL recorded significantly stronger intensity for the 002 peak. The MORD of 002 peak at $\chi = 0°$ for Sb_2Se_3 without seed is around 0.5, while it increased by a factor of 5 for the Sb_2Se_3 + SL. These results agree well with what was found from the TC analysis. Although pole figures showed a similar trend, the increase of intensity of the 002 plane was not as drastic for it to be considered a strongly preferred orientation. At this point, it is worth noting that pole figures for Sb_2Se_3 grown on TiO_2 have not yet been reported. In a recent study by Pattini et al., pole figures were measured for Sb_2Se_3 films grown onto glass, molybdenum, CdS, FTO and ZnO. Among the substrates, strongest texture along the [001] direction was found for the Sb_2Se_3 grown on FTO, proven by strong pole intensity of the 061 peak (Pattini et al., 2020). Considering that, the present study offers an additional view, by means of pole figures, into the grain orientation of the Sb_2Se_3 absorber deployed in the TiO_2/Sb_2Se_3 superstrate configuration.

Texture measurements were also made on individual grains of Sb_2Se_3 + SL film via EBSD. The cross-sectional EBSD map shown in Fig. 4 illustrates that the Sb_2Se_3 layer does not exhibit any preferential growth direction. The average Sb_2Se_3 grain size was found to be around 300–400 nm. This means that not all grains start their growth from the

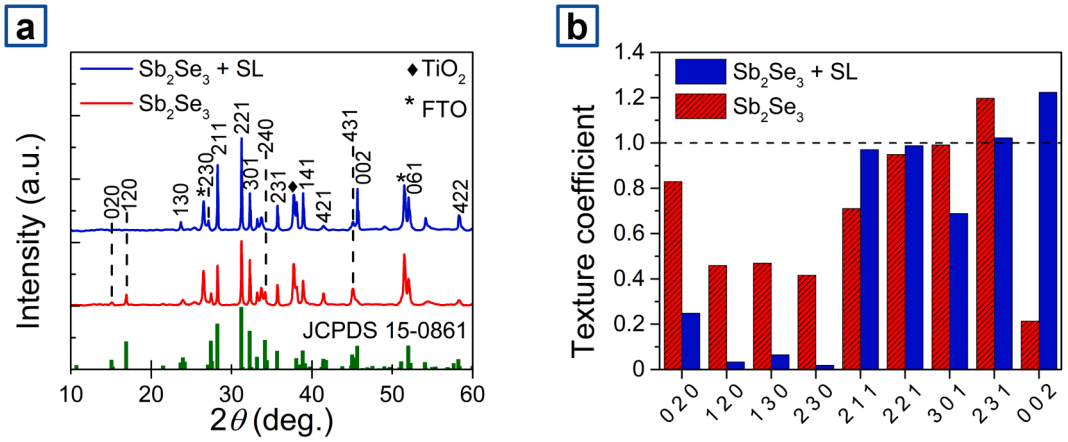

Fig. 2. (a) XRD patterns of FTO/TiO_2/Sb_2Se_3 structures. (b) Texture coefficient values for respective crystal planes in Sb_2Se_3 films.

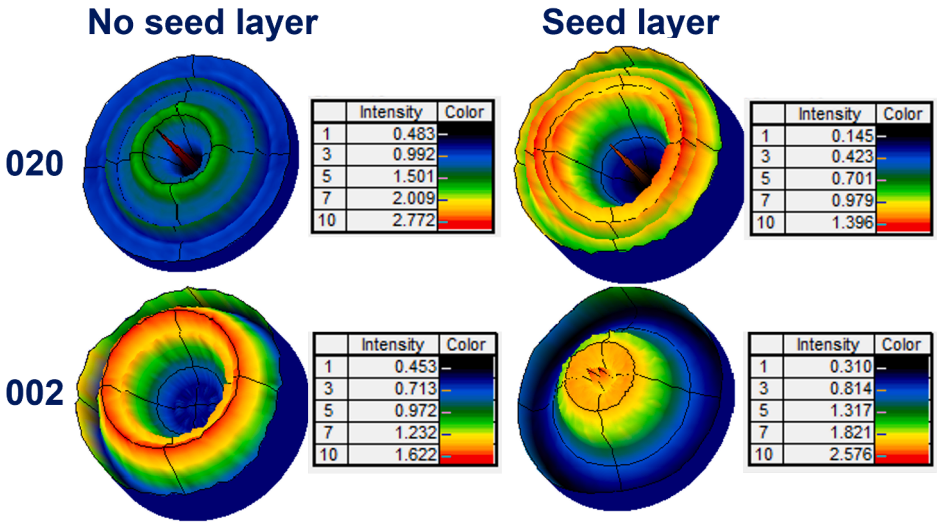

Fig. 3. Pole figures in 020 and 002 projections derived from the XRD measurements of Sb_2Se_3 films grown without and with seed layer onto TiO_2/FTO/glass substrates.

Fig. 4. EBSD map with orientation distribution of the Sb_2Se_3 + SL film (given by false colors, see legend) superimposed on the pattern-quality distribution of the FTO layer. The orientation distribution indicates no pronounced texture of the Sb_2Se_3 + SL layer.

seed layer up to the top and there is still room for improvement. This also relates to achieving favorable grain orientation. Although neither pole figures by XRD nor orientation distribution mapping by EBSD found proof for preferred orientation, clear increase of beneficial 002 peak in Sb_2Se_3 + SL was still detected, which could stem from the increased columnar growth. Hence, it can be argued that further enabling columnar growth would not only increase grain size, but would also enhance texture along the [001] direction. As to the grain orientation, it is now clear the TC analysis is not a trustable tool to determine preferred orientation in the orthorhombic Sb_2Se_3. Instead, careful texture analyses are required to draw strong conclusions on the preferred orientation.

3.2. Device performance and characterization

PV parameters of the solar cells employing Sb_2Se_3 + SL and Sb_2Se_3 without seed layer are listed in Table 1. The schematic of two solar cell configurations is presented in Fig. 5a. The dark and illuminated current density-voltage (*J-V*) curves are shown in Fig. 5b. The curves reveal that the Sb_2Se_3 + SL solar cell shows superior performance compared to the device without seed layer. Improved performance is also reflected from the increase in J_{SC}, V_{OC}, and FF parameters. As has been shown above, the seed layer helped to form columnar compact grains with (hk1) planes, which then seems to correlate with the improvement of PV parameters and device efficiency. In contrast, Sb_2Se_3 without seed layer had dispersed grains with increased presence of (hk0) planes and inferior device performance.

Table 1
Photovoltaic parameters of Sb_2Se_3 solar cells, where V_{OC} is open circuit voltage, J_{SC} is short circuit density, FF is field factor and η is the photoconversion efficiency. * Sb_2Se_3 + SL refers to device employing Sb_2Se_3 on seed layer.

Sample	V_{OC} (V)	J_{SC} (mA cm^{-2})	FF (%)	η (%)
Sb_2Se_3	0.24 ± 0.1	21.1 ± 0.5	35 ± 3	1.6 ± 0.3
Sb_2Se_3 + SL *	0.35 ± 0.1	24.9 ± 0.4	43 ± 2	3.8 ± 0.1

External quantum efficiency (EQE) curves, as shown in Fig. 6a, support the above findings. Throughout the wavelength region from 350 to 1050 nm, Sb_2Se_3 + SL device showed a higher spectral response. This suggests that the columnar microstructure allows more efficient collection of charge carriers, because the density of grain boundaries along the [001] direction is reduced. From the modified EQE plot, the value of the band-gap energy E_g was derived for the 3.7%-efficient Sb_2Se_3 device, shown in Fig. 6b. The band-gap of ~1.25 eV complies well with previous reports (Chen et al., 2015; Grossberg et al., 2020; Hobson et al., 2020).

Despite seed layer deployment allowing notable improvement of the PCE, the 3.7% efficiency is still low compared with the best reported TiO_2/Sb_2Se_3 solar cells (Chen et al., 2017b; Hobson et al., 2020). This means there are still several issues that need to be addressed. Low acceptor density and deep defects in the absorber may possibly limit performance (Chen et al., 2017a; Savory and Scanlon, 2019; Wen et al., 2018).

To gain insight into the carrier density and deep defects in the Sb_2Se_3 absorber, TAS measurement and CV profiling were conducted. As none of the Sb_2Se_3 solar cells grown without seed layer exhibited shunt resistances large enough to measure capacitance, *C*, the results below are presented only for the best seed-assisted device. Capacitance was measured using an equivalent circuit model that includes a capacitor, a series resistor *r* and a resistor in parallel. Series resistance *r* was first extracted from the real part of impedance *Z* (*f*, T) at high frequencies (Levcenko et al., 2016). This was used in the calculation of capacitance from the real and imaginary part of impedance *Z* (*f*, T) signal (Scofield, 1995). The capacitance response entails the response not only from free carriers, but also from bulk and possibly interface defects (Li et al.,

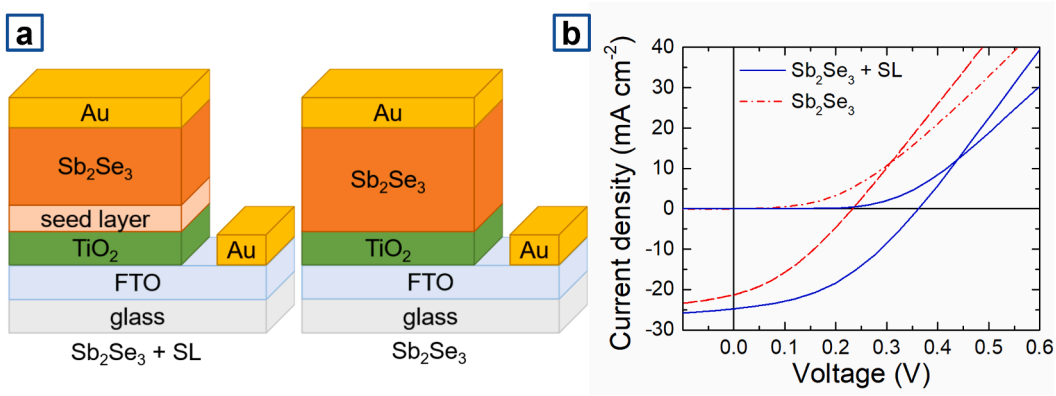

Fig. 5. (a) Sb_2Se_3 + SL and Sb_2Se_3 device configurations and (b) current density–voltage (J-V) curves of the two respective devices.

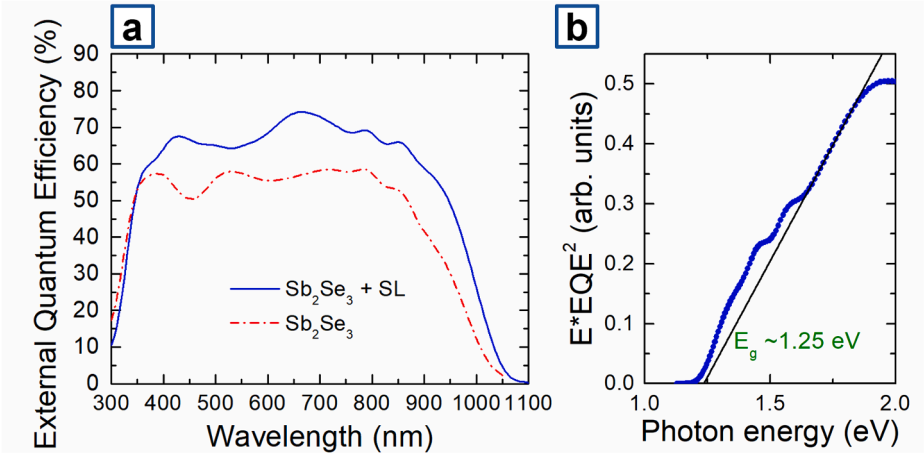

Fig. 6. (a) EQE curves of Sb_2Se_3 solar cells and (b) Band-gap energy of Sb_2Se_3 + SL derived from the modified EQE plot in the long wavelength region.

2019c). Fig. 7a presents the C–*f* curves measured in the temperature range from 80 K to 320 K. The derivatives of the capacitance curves were then taken to determine the relaxation frequencies ω_0, found from the maxima of the $-\omega dC(\omega)/d\omega$ plots, as shown in Fig. 7b. An Arrhenius plot of ω_0 frequencies allows to determine activation energy E_A and thermal emission prefactor ξ_0 of a defect state by using Eq. (2) (Walter et al., 1996):

$$\omega_0 = 2\pi f_0 = 2\xi_0 T^2 exp(-E_A/kT) \quad (2)$$

where ξ_0 is the thermal emission prefactor, k is Boltzmann constant, T is temperature and E_A is activation energy. The Arrhenius plot in Fig. 8 gives a single activation energy of $E_A = 0.39$ eV with thermal emission prefactor ξ_0 of $3 \times 10^6\ s^{-1}\ K^{-2}$. Hu et al., has found activation energies at 0.3–0.4 eV and 0.2–0.6, assigning these to bulk defects (Hu et al., 2019, 2018a, 2018b). Activation energies of 0.39–0.40 eV were also found in both CdS/Sb_2Se_3 and TiO_2/Sb_2Se_3 solar cells (Spalatu et al., 2021). A defect level at 0.48 ± 0.07 eV has been reported in DLTS study, and attributed to a deep acceptor V_{Sb} (Wen et al., 2018). From first-principles calculations, transition energy levels were found for V_{Sb1} and V_{Sb2} acceptor defects, which lay close to 0.39 eV (Huang et al., 2019). DFT study calculated transition energy levels of 0.33 eV and 0.40 eV for Sb_{Se1} and Sb_{Se2} antisite defects, which are deep acceptor defects (Stoliaroff et al., 2020). Also, hybrid DFT study located Sb_{Se1}, Sb_{Se2} and Sb_{Se3} antisite defects close to the 0.39 eV energy (Savory and Scanlon,

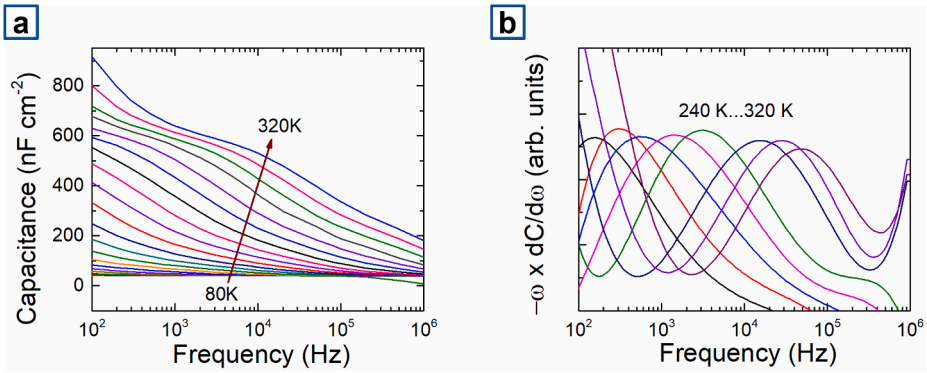

Fig. 7. (a) C-*f*-T curves measured from 80 K to 320 K and (b) –ωdC(ω)/dω vs *f* curves of TiO_2/Sb_2Se_3 solar cell.

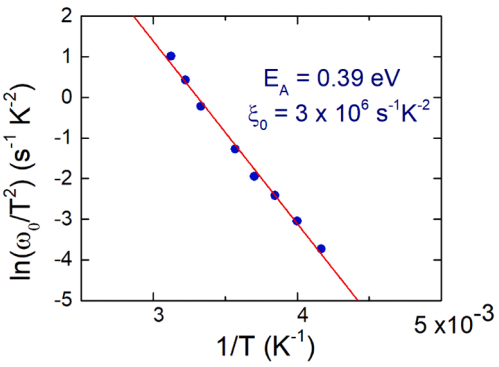

Fig. 8. Arrhenius plot of the inflection frequencies of TiO_2/Sb_2Se_3 device, from which activation energy and thermal emission prefactor were deduced.

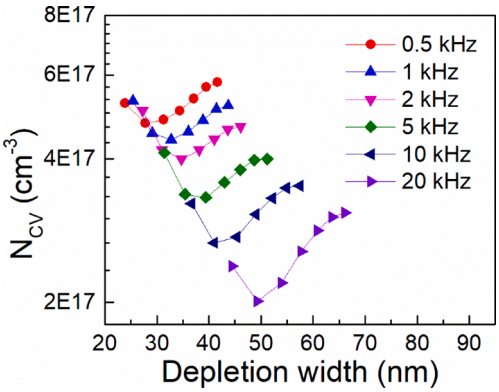

Fig. 9. CV profiles for TiO_2/Sb_2Se_3 solar cell showing carrier density decrease with increasing frequency.

2019). Given that the activation energies of 0.39–0.40 have been found in multiple devices, and the theoretical calculations predicted deep acceptor energy levels close to 0.39 eV, the activation energy obtained in the present study can be assigned to a deep acceptor defect.

To estimate the density of this defect, CV profiles were measured at room temperature. Since the defect band is centered at 10 kHz at room temperature, CV profiles were taken at similar modulation frequencies. Fig. 9 reveals the CV profiles take U-shaped curves, something that is commonly seen in polycrystalline thin film PV devices, and which could be indicative of either deep defect states, back contact barriers or full depletion of the absorber layer caused by large reverse bias (Cabas-Vidani et al., 2018; Eisenbarth et al., 2010; Hadke et al., 2019; Teymur et al., 2021). While the minima of the CV profiles are used to estimate the carrier density, the decrease in the minima values from 4.8×10^{17} to 2.0×10^{17} cm^{-3} also gives a rough estimate over the defect density that could be in the order of 10^{17} cm^{-3}. The free carrier density is estimated to be lower due to the lower values at higher frequencies, but cannot be reliably estimated from this experiment. High resistivities of Sb_2Se_3 absorber films that were determined to lie in the 10^5–10^6 Ω•cm range (Spalatu et al., 2021) indicate that the free carrier density might be substantially lower than the charge densities obtained from CV profiling, which also includes contributions from the deep defects.

From the fact that the admittance spectroscopy results are consistent with the results from CV profiling and that the hot-probe analysis has demonstrated poor, yet clear p-type conductivity for the Sb_2Se_3 absorber films on glass, it can be assumed that the free carrier density stems from this deep acceptor defect. Considering this, the free carrier density can be calculated by using Eq. (3) (Sze and Ng, 2006; Teymur et al., 2021):

$$p = 1 \Big/ \sqrt{2} \times (N_V N_A)^{1/2} exp(-E_A/2kT) \quad (3)$$

where N_V is the effective density of states of valence band, taken to be 1×10^{19} cm^{-3}, N_A is 2.0×10^{17} cm^{-3}, which is the carrier density taken from CV analysis and E_A is 0.39 eV, that was found in TAS analysis.

The free carrier density calculated at room temperature gives $\sim 5 \times 10^{14}$ cm^{-3}, which is significantly lower than the total charge densities estimated from the CV profiles. This is higher than the free carrier density of 1.8×10^{13} cm^{-3} reported for the intrinsic Sb_2Se_3 films (Chen et al., 2017a). Nevertheless, the carrier density below 10^{15} explains the large Sb_2Se_3 resistivity (Spalatu et al., 2021) and the fact Sb_2Se_3 cannot be measured with Hall measurement technique (Chen et al., 2017a; Hobson et al., 2020). Overall, this finding illustrates that in addition to further optimization of the Sb_2Se_3 microstructure, extrinsic doping steps, such as with copper, tin or halogenides, must be introduced to address low free carrier density and high density of defects.

4. Conclusion

In the present study, we performed careful analysis on the grain orientation and deep defects in Sb_2Se_3 solar cells fabricated by close-spaced sublimation. Through the combination of pole figures measured by XRD and orientation distribution maps performed by EBSD, we refined the understanding of grain orientation in the emerging Sb_2Se_3 thin film solar cell absorber. The microstructures of two thin films were compared, i.e. Sb_2Se_3 grown on a TiO_2 seed layer and plain Sb_2Se_3 without any seed layer. The seed-assisted Sb_2Se_3 film exhibited more compact, columnar grains and significantly stronger texture along the [001] direction, as compared with the plain Sb_2Se_3, which had dispersed grain structure and a measurable texture along the [010] direction. The seed-assisted Sb_2Se_3 devices performed clearly better, which was attributed to the improved absorber microstructure, enhancing charge transport across the absorber layer. Our results indicate that the seed layer deployment serves as one of the processing routes for attaining preferential Sb_2Se_3 growth along the [001] direction. The present study also investigated the free carrier density and deep defects in the absorber by performing CV and TAS measurements on the seed-assisted Sb_2Se_3 device. TAS analysis revealed an activation energy of 0.39 eV that was assigned to a deep acceptor defect. From CV profiles, the sum of defect and the free carrier density were estimated to be at $\sim 10^{17}$ cm^{-3}. Free carrier density that was calculated from the deep defect band revealed a significantly lower value of $\sim 5 \times 10^{14}$ cm^{-3}. This value is consistent with large resistivities shown by intrinsic Sb_2Se_3 films. This in turn shows the defect density in the Sb_2Se_3 device could be in the order of 10^{17} cm^{-3}. Overall, the present study demonstrated that both, structural and optoelectronic properties, require additional processing routes, such as post deposition treatments and doping, to substantially boost the Sb_2Se_3 solar cell efficiency.

Declaration of Competing Interest

The authors declare that they have no known competing financial interests or personal relationships that could have appeared to influence the work reported in this paper.

Acknowledgements

This study was funded by the Estonian Research Council project PRG627 “Antimony chalcogenide thin films for next-generation semi-transparent solar cells applicable in electricity producing windows”, the Estonian Research Council project PSG689 “Bismuth Chalcogenide Thin-Film Disruptive Green Solar Technology for Next Generation Photovoltaics”, the Estonian Centre of Excellence project TK141 (TAR16016EK) “Advanced materials and high-technology devices for energy recuperation system”, and the EU H2020 program under the ERA Chair project 5GSOLAR grant agreement No 952509. R. Krautmann acknowledges Archimedes Foundation for financing the PhD student mobility through the Dora Plus program.

References

Abou-Ras, D., Bär, M., Caballero, R., Gunder, R., Hages, C., Heinemann, M.D., Kaufmann, C.A., Krause, M., Levcenko, S., Mainz, R., Márquez, J., Nikolaeva, A., Redinger, A., Schäfer, N., Schorr, S., Stange, H., Unold, T., Wilks, R.G., 2018. Advanced characterization and in-situ growth monitoring of Cu(In, Ga)Se2 thin films and solar cells. Sol. Energy 170, 102–112. https://doi.org/10.1016/j.solener.2018.04.032.

Ariosa, D., Elhordoy, F., Dalchiele, E.A., Marotti, R.E., Stari, C., 2011. Texture vs morphology in ZnO nano-rods: On the x-ray diffraction characterization of electrochemically grown samples. J. Appl. Phys. 110 (12), 124901. https://doi.org/10.1063/1.3669026.

Bérubé, L.P., L'Espérance, G., 1989. A Quantitative Method of Determining the Degree of Texture of Zinc Electrodeposits. J. Electrochem. Soc. 136 (8), 2314–2315. https://doi.org/10.1149/1.2097318.

Cabas-Vidani, A., Haass, S.G., Andres, C., Caballero, R., Figi, R., Schreiner, C., Márquez, J.A., Hages, C., Unold, T., Bleiner, D., Tiwari, A.N., Romanyuk, Y.E., 2018. High-Efficiency (Li $_x$ Cu $_{1-x}$) $_2$ ZnSn(S, Se) 4 Kesterite Solar Cells with Lithium Alloying. Adv. Energy Mater. 8 (34), 1801191. https://doi.org/10.1002/aenm.201801191.

Chen, C., Bobela, D.C., Yang, Y.e., Lu, S., Zeng, K., Ge, C., Yang, B.o., Gao, L., Zhao, Y., Beard, M.C., Tang, J., 2017a. Characterization of basic physical properties of Sb2Se3 and its relevance for photovoltaics. Front. Optoelectron. 10 (1), 18–30. https://doi.org/10.1007/s12200-017-0702-z.

Chen, C., Zhao, Y., Lu, S., Li, K., Li, Y., Yang, B.o., Chen, W., Wang, L., Li, D., Deng, H., Yi, F., Tang, J., 2017b. Accelerated Optimization of TiO $_2$ /Sb $_2$ Se $_3$ Thin Film Solar Cells by High-Throughput Combinatorial Approach. Adv. Energy Mater. 7 (20), 1700866. https://doi.org/10.1002/aenm.201700866.

Chen, C., Li, W., Zhou, Y., Chen, C., Luo, M., Liu, X., Zeng, K., Yang, B.o., Zhang, C., Han, J., Tang, J., 2015. Optical properties of amorphous and polycrystalline Sb2Se3 thin films prepared by thermal evaporation. Appl. Phys. Lett. 107 (4), 043905. https://doi.org/10.1063/1.4927741.

Eensalu, J.S., Katerski, A., Kärber, E., Weinhardt, L., Blum, M., Heske, C., Yang, W., Oja Acik, I., Krunks, M., 2019. Semitransparent Sb2S3 thin film solar cells by ultrasonic spray pyrolysis for use in solar windows. Beilstein J. Nanotechnol. 10, 2396–2409. https://doi.org/10.3762/bjnano.10.230.

Eisenbarth, T., Unold, T., Caballero, R., Kaufmann, C.A., Schock, H.-W., 2010. Interpretation of admittance, capacitance-voltage, and current-voltage signatures in Cu(In, Ga)Se2 thin film solar cells. J. Appl. Phys. 107 (3), 034509. https://doi.org/10.1063/1.3277043.

Ghosh, G., 1993. The sb-se (antimony-selenium) system. J. Phase Equilibria 14 (6), 753–763. https://doi.org/10.1007/BF02667889.

Grossberg, M., Volobujeva, O., Penežko, A., Kaupmees, R., Raadik, T., Krustok, J., 2020. Origin of photoluminescence from antimony selenide. J. Alloys Compd. 817, 152716. https://doi.org/10.1016/j.jallcom.2019.152716.

Hadke, S., Levcenko, S., Sai Gautam, G., Hages, C.J., Márquez, J.A., Izquierdo-Roca, V., Carter, E.A., Unold, T., Wong, L.H., 2019. Suppressed Deep Traps and Bandgap Fluctuations in Cu $_2$ CdSnS $_4$ Solar Cells with ≈8% Efficiency. Adv. Energy Mater. 9 (45), 1902509. https://doi.org/10.1002/aenm.v9.4510.1002/aenm.201902509.

Hobson, T.D.C., Phillips, L.J., Hutter, O.S., Shiel, H., Swallow, J.E.N., Savory, C.N., Nayak, P.K., Mariotti, S., Das, B., Bowen, L., Jones, L.A.H., Featherstone, T.J., Smiles, M.J., Farnworth, M.A., Zoppi, G., Thakur, P.K., Lee, T.-L., Snaith, H.J., Leighton, C., Scanlon, D.O., Dhanak, V.R., Durose, K., Veal, T.D., Major, J.D., 2020. Isotype Heterojunction Solar Cells Using n-Type Sb2Se3 Thin Films. Chem. Mater. https://doi.org/10.1021/acs.chemmater.0c00223.

Hu, X., Tao, J., Chen, S., Xue, J., Weng, G., Kaijiang, Hu, Z., Jiang, J., Chen, S., Zhu, Z., Chu, J., 2018a. Improving the efficiency of Sb2Se3 thin-film solar cells by post annealing treatment in vacuum condition. Sol. Energy Mater. Sol. Cells 187, 170–175. https://doi.org/10.1016/j.solmat.2018.08.006.

Hu, X., Tao, J., Wang, Y., Xue, J., Weng, G., Zhang, C., Chen, S., Zhu, Z., Chu, J., 2019. 5.91%-efficient Sb2Se3 solar cells with a radio-frequency magnetron-sputtered CdS buffer layer. Appl. Mater. Today 16, 367–374. https://doi.org/10.1016/j.apmt.2019.06.001.

Hu, X., Tao, J., Weng, G., Jiang, J., Chen, S., Zhu, Z., Chu, J., 2018b. Investigation of electrically-active defects in Sb2Se3 thin-film solar cells with up to 5.91% efficiency via admittance spectroscopy. Sol. Energy Mater. Sol. Cells 186, 324–329. https://doi.org/10.1016/j.solmat.2018.07.004.

Huang, M., Xu, P., Han, D., Tang, J., Chen, S., 2019. Complicated and Unconventional Defect Properties of the Quasi-One-Dimensional Photovoltaic Semiconductor Sb 2 Se 3. ACS Appl. Mater. Interfaces 11 (17), 15564–15572. https://doi.org/10.1021/acsami.9b0122010.1021/acsami.9b01220.s001.

Levcenko, S., Just, J., Redinger, A., Larramona, G., Bourdais, S., Dennler, G., Jacob, A., Unold, T., 2016. Deep Defects in Cu2ZnSn (S, Se)4 Solar Cells with Varying Se Content. Phys. Rev. Appl. 5, 024004 https://doi.org/10.1103/PhysRevApplied.5.024004.

Li, G., Li, Z., Liang, X., Guo, C., Shen, K., Mai, Y., 2019a. Improvement in Sb 2 Se 3 Solar Cell Efficiency through Band Alignment Engineering at the Buffer/Absorber Interface. ACS Appl. Mater. Interfaces 11 (1), 828–834. https://doi.org/10.1021/acsami.8b1761110.1021/acsami.8b17611.s001.

Li, K., Chen, C., Lu, S., Wang, C., Wang, S., Lu, Y., Tang, J., 2019b. Orientation Engineering in Low-Dimensional Crystal-Structural Materials via Seed Screening. Adv. Mater. 31 (44), 1903914. https://doi.org/10.1002/adma.v31.4410.1002/adma.201903914.

Li, Z., Chen, X., Zhu, H., Chen, J., Guo, Y., Zhang, C., Zhang, W., Niu, X., Mai, Y., 2017. Sb2Se3 thin film solar cells in substrate configuration and the back contact selenization. Sol. Energy Mater. Sol. Cells 161, 190–196. https://doi.org/10.1016/j.solmat.2016.11.033.

Li, Z., Liang, X., Li, G., Liu, H., Zhang, H., Guo, J., Chen, J., Shen, K., San, X., Yu, W., Schropp, R.E.I., Mai, Y., 2019c. 9.2%-efficient core-shell structured antimony selenide nanorod array solar cells. Nat. Commun. 10, 1–9. https://doi.org/10.1038/s41467-018-07903-6.

Liang, X., Guo, C., Liu, T., Liu, Y., Yang, L., Song, D., Shen, K., Schropp, R.E.I., Li, Z., Mai, Y., 2020. Crystallographic Orientation Control of 1D Sb $_2$ Se $_3$ Nanorod Arrays for Photovoltaic Application by In Situ Back-Contact Engineering. Sol. RRL 4 (10), 2000294. https://doi.org/10.1002/solr.v4.1010.1002/solr.202000294.

Liu, X., Chen, J., Luo, M., Leng, M., Xia, Z., Zhou, Y., Qin, S., Xue, D.-J., Lv, L.u., Huang, H., Niu, D., Tang, J., 2014. Thermal evaporation and characterization of Sb2Se3 thin film for substrate Sb2Se3/CdS solar cells. ACS Appl. Mater. Interfaces 6 (13), 10687–10695. https://doi.org/10.1021/am502427s.

Liu, X., Xiao, X., Yang, Y.e., Xue, D.-J., Li, D.-B., Chen, C., Lu, S., Gao, L., He, Y., Beard, M.C., Wang, G., Chen, S., Tang, J., 2017. Enhanced Sb $_2$ Se $_3$ solar cell performance through theory-guided defect control. Prog. Photovolt. Res. Appl. 25 (10), 861–870. https://doi.org/10.1002/pip.v25.1010.1002/pip.2900.

Pattini, F., Rampino, S., Mezzadri, F., Calestani, D., Spaggiari, G., Sidoli, M., Delmonte, D., Sala, A., Gilioli, E., Mazzer, M., 2020. Role of the substrates in the ribbon orientation of Sb2Se3 films grown by Low-Temperature Pulsed Electron Deposition. Sol. Energy Mater. Sol. Cells 218, 110724. https://doi.org/10.1016/j.solmat.2020.110724.

Savory, C.N., Scanlon, D.O., 2019. The complex defect chemistry of antimony selenide †. https://doi.org/10.1039/c9ta02022e.

Scofield, J.H., 1995. Effects of series resistance and inductance on solar cell admittance measurements. Sol. Energy Mater. Sol. Cells 37 (2), 217–233. https://doi.org/10.1016/0927-0248(95)00016-X.

Spalatu, N., Krautmann, R., Katerski, A., Karber, E., Josepson, R., Hiie, J., Acik, I.O., Krunks, M., 2021. Screening and optimization of processing temperature for Sb2Se3 thin film growth protocol: Interrelation between grain structure, interface intermixing and solar cell performance. Sol. Energy Mater. Sol. Cells 225, 111045. https://doi.org/10.1016/j.solmat.2021.111045.

Spalatu, N., Krunks, M., Hiie, J., 2017. Structural and optoelectronic properties of CdCl2 activated CdTe thin films modified by multiple thermal annealing. Thin Solid Films 633, 106–111. https://doi.org/10.1016/j.tsf.2016.09.042.

Stoliaroff, A., Lecomte, A., Rubel, O., Jobic, S., Zhang, XiangHua, Latouche, C., Rocquefelte, X., 2020. Deciphering the Role of Key Defects in Sb2Se3, a Promising Candidate for Chalcogenide-Based Solar Cells. ACS Appl. Energy Mater. 3 (3), 2496–2509. https://doi.org/10.1021/acsaem.9b0219210.1021/acsaem.9b02192.s001.

Sze, S.M., Ng, K.K., 2006. Physics of Semiconductor Devices. John Wiley & Sons, Inc., Hoboken, NJ, USA.

Tang, R., Zheng, Z.-H., Su, Z.-H., Li, X.-J., Wei, Y.-D., Zhang, X.-H., Fu, Y.-Q., Luo, J.-T., Fan, P., Liang, G.-X., 2019. Highly efficient and stable planar heterojunction solar cell based on sputtered and post-selenized Sb2Se3 thin film. Nano Energy 64, 103929. https://doi.org/10.1016/j.nanoen.2019.103929.

Teymur, B., Levcenco, S., Hempel, H., Bergmann, E., Márquez, J.A., Choubrac, L., Hill, I. G., Unold, T., Mitzi, D.B., 2021. Optoelectronic and material properties of solution-processed Earth-abundant Cu2BaSn(S, Se)4 films for solar cell applications. Nano Energy 80, 105556. https://doi.org/10.1016/j.nanoen.2020.105556.

Walter, T., Herberholz, R., Müller, C., Schock, H.W., 1996. Determination of defect distributions from admittance measurements and application to Cu(In,Ga)Se2 based heterojunctions Determination of defect distributions from admittance measurements and application to Cu(In,Ga)Se2 based heterojunctions. J. Appl. Phys. 80, 4411–4420. https://doi.org/10.1063/1.363401.

Wang, L., Li, D.B., Li, K., Chen, C., Deng, H.X., Gao, L., Zhao, Y., Jiang, F., Li, L., Huang, F., He, Y., Song, H., Niu, G., Tang, J., 2017. Stable 6%-efficient Sb2Se3 solar cells with a ZnO buffer layer. Nat. Energy 2, 17046. https://doi.org/10.1038/nenergy.2017.46.

Wang, Y., Li, J., Chen, Y., Zhou, J., Zhang, J., Mao, W., Zheng, S., Pan, Y., Liu, Y., Dai, K., Hu, X., Tao, J., Weng, G., Jiang, J., Chen, S., Chu, J., 2020. Effects of working pressure and power on photovoltaic and defect properties of magnetron sputtered Sb 2 Se 3 thin-film solar cells. Appl. Opt. 59 (4), 948. https://doi.org/10.1364/AO.382805.

Wen, X., Chen, C., Lu, S., Li, K., Kondrotas, R., Zhao, Y., Chen, W., Gao, L., Wang, C., Zhang, J., Niu, G., Tang, J., 2018. Vapor transport deposition of antimony selenide thin film solar cells with 7.6% efficiency. Nat. Commun. 9, 1–10. https://doi.org/10.1038/s41467-018-04634-6.

Zhang, H., Yuan, S., Deng, H., Ishaq, M., Yang, X., Hou, T., Shah, U.A., Song, H., Tang, J., 2020. Controllable orientations for Sb2S3 solar cells by vertical VTD method. Prog. Photovolt. Res. Appl. 28 (8), 823–832. https://doi.org/10.1002/pip.v28.810.1002/pip.3278.

Zhou, H., Feng, M., Li, P., Gong, X., Zhang, D., Chen, S., 2020. Fabrication of a preferentially [001]-oriented Sb2Se3thin film on diverse substrates and its application in photoelectrochemical water reduction. Sustain. Energy Fuels 4 (8), 3943–3950. https://doi.org/10.1039/D0SE00646G.

Zhou, Y., Leng, M., Xia, Z., Zhong, J., Song, H., Liu, X., Yang, B.o., Zhang, J., Chen, J., Zhou, K., Han, J., Cheng, Y., Tang, J., 2014. Solution-processed antimony selenide heterojunction solar cells. Adv. Energy Mater. 4 (8), 1301846. https://doi.org/10.1002/aenm.201301846.